On the formation of an inverted weathering profile on Mount Kilimanjaro, Tanzania: Buried paleosol or groundwater weathering?

Mark Gabriel Little *, Cin-Ty Aeolus Lee

Department of Earth Sciences, MS-126, Rice University, 6100 Main Street, Houston, TX 77005, USA

Abstract

This paper presents an investigation into the degree and nature of chemical weathering during soil formation on a volcanic (phonolite) substrate on the southern slopes of Mt. Kilimanjaro in northern Tanzania. The high field strength elements Nb and Ta were used to estimate enrichments and depletions relative to the bedrock. The degree of weathering was found to increase with depth in the soil profile. At depths greater than 200 cm, Si, Na, K, Ca, and Mg have been depleted by nearly 100% while Al has been enriched, resulting in a highly aluminous soil residue (40–50 wt.% Al_2O_3). At depths shallower than 200 cm, the soil is also depleted in Si, Na, K, Ca and Mg though not to the extents seen at depths greater than 200 cm. The lower degrees of weathering in the upper 200 cm are also evidenced by the fact that the layer above 200 cm is characterized by slight positive Eu anomalies relative to other rare earth elements whereas the deeper layer exhibits no Eu anomalies. The rare earth element systematics are consistent with preferential weathering of the glassy matrix in the upper 200 cm, leaving behind plagioclase phenocrysts, which are enriched in Eu. In the deeper layer, weathering appears to be so extensive that both Eu-rich plagioclase phenocrysts and Eu-poor glass/ash have largely weathered away. These observations collectively show that the upper and lower layers of the weathering profile have undergone different weathering histories. Four scenarios may explain the apparent inverted weathering profile: re-precipitation followed by erosion, Aeolian deposition, a buried paleosol, and enhanced weathering due to lateral subsurface water flow. The first hypothesis fails to explain the massive losses of Si, Na, K, Ca, and Mg below 200 cm. The Aeolian deposition hypothesis is also untenable because it contradicts the trace element and REE's behaviors. The latter two hypotheses are both reasonable; however, the buried paleosol model is inconsistent with some physical and geochemical observations and the subsurface flow model requires the influence of hydraulic conditions not tested in this study. It is concluded here that either the buried paleosol model or the subsurface flow model can explain the formation of the Machame soils with the latter having novel implications for the transport of dissolved cations to the ocean.
© 2006 Elsevier B.V. All rights reserved.

Keywords: Soil formation; Subsurface water; Chemical weathering; Tanzania

1. Introduction

Quantifying the rate of continental weathering is of fundamental importance for understanding atmospheric CO$_2$ drawdown (Berner et al., 1983; Berner, 1995) and the magnitude of the fluxes of various elements into the marine environment, many of which have paleo-oceanographic significance (Gaillardet et al., 1999; Kump et al., 2000; Sak et al., 2003). In a quasi-steady-state system, the continental weathering flux can, in theory, be estimated anywhere along the pathway between the source and the

---

* Corresponding author.
E-mail address: mglittle@rice.edu (M.G. Little).

sink, the latter represented by marine sediments and the former represented by chemical weathering of the continents. This means that one approach in measuring the continental weathering flux is to measure the flux of solutes into the marine environment at the mouths of major river systems (Gaillardet et al., 1999; Dessert et al., 2001). This approach is convenient because the watershed areas of large river systems effectively average over large regions of continental crust, and as such, are believed to be fairly representative of average continental weathering rates. Thus, if the goal is to quantify global weathering rates and fluxes into the marine environment on large scales, the riverine perspective should be sufficient. However, if the goal is to better understand the mechanisms of continental weathering, the averaging effect of rivers is no longer a benefit. To understand the mechanisms of continental weathering, attention must then be focused toward understanding the source terms in addition to the riverine fluxes.

In this context, the most obvious source term to turn to is the chemical weathering flux associated with soil formation on either stable geomorphic surfaces (non-eroding) or steady-state landforms, where erosion and conversion of bedrock to soil roughly balance. However, other source terms may also exist. For example, subsurface water flow may result in chemical weathering of the deep subsurface, but its significance in the global context is unclear largely because of the greater inaccessibility of the deep subsurface compared to soil profiles. Nevertheless, recent studies seem to hint that subsurface water flow may contribute to the chemical weathering flux of continents (Basu et al., 2001). If such subsurface water is significant and bypasses the river mouth by directly entering the oceans, the solute flux measured at river mouths may underestimate the true continental weathering flux to oceans for some elements.

We investigated a young, but unusually mature weathering profile situated on an intermediate volcanic substrate on the southern slopes of Mt. Kilimanjaro in northeastern Tanzania, a region having a tropical equatorial climate. This weathering profile was fortuitously exposed by a road cut, affording access to the deep, and otherwise inaccessible, portions of the weathering profiles in this region. Importantly, in this weathering profile, the degree of weathering appears to be greatest at depth, which is the inverse of what is seen in typical soil profiles where weathering is top–down. We argue here that this inverted profile may be the result of a buried paleosol or enhanced chemical weathering at depth due to focused subsurface lateral water flow. The latter interpretation, if correct, would underscore the importance of subsurface water weathering at least locally.

2. Study area and description of weathering profile

Samples were collected from a road cut-exposed weathering profile (03°11.275′ S, 37°14.157′ E, elevation 1639 m) in the Machame region of northern Tanzania on the southern slope of Mt. Kilimanjaro (Fig. 1). The andosols in this region were formed on phonolitic lava and ash flows. The weathering profile examined in this study is situated on a relatively undissected surface, which suggests relatively little erosion. Most erosion is confined to isolated ravines bordering large swathes of non-eroding geomorphic surfaces. The studied weathering profile is situated on the edge of one of these uneroded geomorphic surfaces and has been conveniently exposed as a consequence of a deep ravine and a road cut. Lava flows on the southern slope of Kilimanjaro have been dated between roughly 0.17 to 0.51 Ma (Evernden and Curtis, 1965; Dawson, 1992). The modern, average annual rainfall in the Machame region is 1929 mm/year (Anderson, 1982).

The relatively unweathered protolith of the Machame soils is a bluish-gray lithified welded ash of phonolitic composition. We obtained a sample of the protolith from blocks of bedrock exposed near the base of the roadcut. The groundmass of the protolith is largely aphanitic ($\sim 90\%$ of thin section area) and is dominated by small plagioclase lathes and tiny dark green to black grains of magnetite–ulvospinel. Occasional phenocrysts are olivines with some of those having alteration rims of iddingsite. The thickness of the sampled weathering profile is ~ 5 m and consists of three main horizons (from bottom to top): a dark gray, semi-consolidated saprolite composed of gibbsite gravel and weathered clasts; a friable, grayish brown, aluminum rich gravel with large voids; and a dark brown, organic rich, sandy loam layer. A
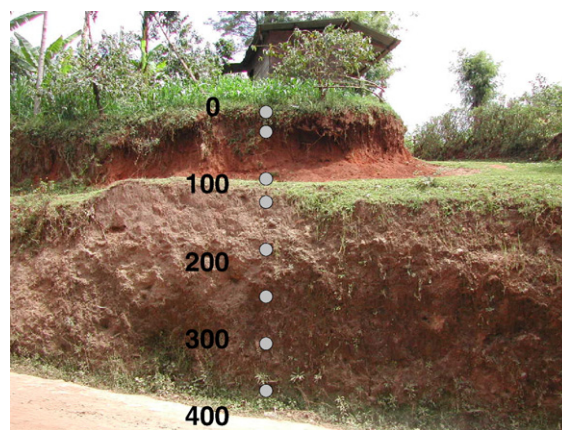

Fig. 1. Road cut in the Machame region of Tanzania on the southern slopes of Mt. Kilimanjaro. The gray circles indicate the approximate depths at which samples were taken.

very shallow Oi horizon, less than 5 cm thick, consisting primarily of forest litter, was also present, but not sampled. We collected 8 soil samples at 30–60 cm intervals down to a maximum depth of ~370 cm.

3. Methods

Machame soil and protolith samples were dried for 24 h at 105 °C. Samples were then ground by hand with a ceramic mortar and pestle. Six grams of each sample powder and USGS rock powder standards BHVO1, BHVO2, and BIR1 were sent to Washington State University at Pullman's GeoAnalytical Lab for XRF determination of Si, Ti, Al, Fe, Mn, Mg, Ca, Na, K, and P concentrations and for determination of Loss on Ignition (LOI), defined as the fraction of mass lost after heating each sample for 16 h at 900 °C (Johnson et al., 1999; Cornelius, 2004).

Sample powders, a blank, and BHVO1, BHVO2, and BIR1 USGS rock standards were prepared for inductively coupled plasma mass spectrometry (ICP-MS) analysis at Rice University using a series of acid dissolutions. Approximately 80 mg of the Machame soil and rock powders, BHVO2, and BIR1 were weighed; 2 aliquots of approximately 40 and 80 mg of BHVO1 were weighed for use as an external standard. Powders were placed in Teflon beakers with approximately 0.5 mL each of concentrated Seastar HNO_3 and $HClO_4$. These solutions were sealed and ultrasonicated for ~20 min. Beakers were then heated overnight at 115 °C. The following day, beakers were removed from the oven, unsealed, and placed on heating pads at ~175 °C until the solutions had dried down. This process of adding acids, overnight heating, and drying down was repeated 2 additional times; once again with

the addition of 0.5 mL each of concentrated HNO_3 and $HClO_4$ and finally with the addition of 1.0 mL of $HClO_4$ only.

Following the third and final dry down, ~1 mL of 2% HNO3 was added to the samples. Beakers were placed on a hot plate at ~100 °C for about 2 h. Approximately 280 μL of a 440.81 ppb indium solution (to serve as an internal standard) was precisely weighed into a 125 mL capacity, low density polyethylene bottle. The contents of the Teflon beakers were carefully washed into the polyethylene bottles using dilute HNO_3. A small drop of 1 M HCl was added to keep the dissolved Fe in solution. The contents of the bottles were then diluted up to 100 mL (~1 ppb indium in the final solution) with dilute HNO_3 and weighed again.

Machame samples, blank, BHVO1, BHVO2, and BIR1 were all run on a Finnigan Element II, single collector ICP-MS at Rice University. The ICP-MS was run in low and medium resolution modes ($m / \Delta m = 300$, 4000), the latter allowing for the analysis of Na, Mg, Al, P, K, Ca, Sc, Ti, V, Cr, Mn, Fe, Co, Ni, Cu, Zn, Zr, and Nb, for which isobaric molecular interferences can occasionally be a problem in low resolution. The In values were used to correct for instrumental drift. The procedural blank was used to correct for blanks introduced during the dissolution process. The external precision is <3%.

4. Results

The concentration data from the XRF analysis were consistent with the ICP-MS data for the major elements. For internal consistency, we report only ICP-MS data in Tables 1 and 2 (with the exception of Si which is lost as volatile SiF_4 during our dissolution process). The partly

Table 1
LOI-corrected major element oxide concentrations

Wt.%	5 cm	30	91	122	183	244	305	366	Protolith
LOI	33.25	31.84	29.94	31.38	32.96	28.34	27.67	28.63	7.95
Na_2O	0.38	0.35	0.38	0.35	0.27	0.05	0.11	0.12	4.42
MgO	0.76	0.67	0.73	0.66	0.67	0.30	0.33	0.26	1.11
Al_2O_3	30.17	30.08	31.16	30.07	41.20	65.03	67.09	79.59	25.90
SiO_2[a]	30.51	30.31	30.37	30.32[b]	24.45	5.38[b]	3.53	4.44	56.78
P_2O_5	1.09	1.06	1.09	1.00	0.80	0.52	0.63	0.72	0.36
K_2O	0.78	0.72	0.74	0.73	0.55	0.09	0.13	0.09	7.17
CaO	0.59	0.51	0.60	0.50	0.37	0.03	0.03	0.04	1.89
TiO_2	4.32	3.99	4.27	3.83	3.62	2.18	2.78	2.46	1.31
MnO	0.18	0.17	0.18	0.16	0.19	0.24	0.32	0.34	0.25
FeO	17.49	16.97	17.96	16.79	16.22	12.11	15.20	14.46	7.29
Total	86.26	84.82	87.47	84.40	88.35	85.93	90.15	102.51	106.49

All values determined using medium resolution ICP-MS unless indicated.
[a] Values determined by XRF.
[b] Values interpolated due to problems in XRF.

Table 2
Minor and trace element concentrations by depth

ppm	5 cm	30	91	122	183	244	305	366	Protolith
Li	15.9	16.1	17.9	16.8	25.0	45.6	63.2	56.2	54.1
Be	2.00	1.94	1.99	2.00	1.95	1.49	1.17	1.36	13.0
Sc[a]	12.7	13.0	13.7	12.6	15.4	11.3	13.8	15.2	8.62
V[a]	173	170	178	167	141	9.51	6.44	4.45	2.98
Cr[a]	138	127	136	129	103	5.71	4.50	3.66	3.47
Co[a]	11.5	10.7	11.5	9.98	9.13	5.32	5.11	9.32	4.34
Ni[a]	22.9	22.3	23.3	22.2	19.2	33.2	10.4	2.20	0.52
Cu[a]	307	99.3	38.6	31.4	18.7	10.4	11.5	11.0	9.43
Zn[a]	186	137	116	110	111	164	207	197	288
Ga	42.3	41.8	45.5	45.4	43.7	61.1	66.7	71.9	41.9
Rb	23.79	22.1	23.0	23.7	15.6	4.03	5.77	4.40	211
Sr	128	119	136	127	75.4	10.5	5.19	3.51	128
Y	18.7	17.5	19.1	19.4	13.2	8.23	8.66	8.63	64.87
Zr[a]	1420	1520	1520	1390	1900	2850	3570	3480	2200
Nb[a]	398	410	446	399	480	678	855	796	517
Cs	2.11	1.98	2.11	2.12	1.41	0.130	0.153	0.128	2.14
Ba	274	282	296	282	185	183	60.1	36.2	705
La	51.7	49.3	54.5	57.5	42.6	90.3	86.9	69.5	228
Ce	240	219	243	241	293	345	332	425	394
Pr	11.0	10.5	11.6	11.6	8.22	9.33	9.02	7.69	37.7
Nd	41.6	37.4	40.0	41.4	29.7	22.3	20.9	18.6	108
Sm	7.96	7.50	8.06	7.86	5.93	2.84	2.74	2.64	17.6
Eu	2.23	2.12	2.27	2.27	1.58	0.54	0.49	0.49	3.69
Tb	0.927	0.882	0.951	0.960	0.682	0.397	0.385	0.380	2.19
Gd	6.24	5.87	6.29	6.39	4.45	2.24	2.13	2.05	14.3
Dy	4.80	4.57	4.90	4.91	3.55	2.15	2.13	2.09	11.8
Ho	0.807	0.765	0.817	0.823	0.602	0.379	0.395	0.382	2.12
Er	2.20	2.09	2.21	2.24	1.71	1.15	1.23	1.21	6.28
Tm	0.323	0.311	0.330	0.328	0.269	0.187	0.203	0.195	0.981
Yb	2.16	2.08	2.16	2.16	1.92	1.27	1.36	1.34	6.59
Lu	0.277	0.266	0.277	0.277	0.249	0.162	0.170	0.171	0.943
Hf	24.1	24.0	24.8	24.6	30.4	49.7	58.1	50.7	34.0
Ta	21.8	22.5	24.7	23.1	25.5	40.1	50.1	41.4	26.1
Tl	0.218	0.217	0.226	0.229	0.156	0.0376	0.0283	0.0367	0.114
Pb	52.4	50.7	52.3	52.3	44.7	21.3	24.5	19.6	15.0
Th	52.4	51.8	55.7	53.9	56.9	74.8	87.6	77.5	56.4
U	9.50	9.43	10.0	9.76	10.8	23.9	21.7	22.4	9.09

All values determined using low resolution ICP-MS unless indicated.
[a] Values determined using medium resolution ICP-MS.

unweathered protolith (i.e., bedrock) has 52 wt.% SiO_2, 7.2% K_2O, 4.4% Na_2O, and 26% Al_2O_3 with an Mg# (Mg/(Mg+Fe)×100) of 21. The intermediate SiO_2 contents and high total alkali contents classifies this protolith as a phonolitic tephrite. We note, however, that this protolith appears to have unusually high Al_2O_3 and low Mg# compared to magmatic rocks having similar SiO_2 contents (Al_2O_3 contents typically range between 15–20 wt.%). The low Mg# of this rock is likely due to extensive crystallization of mafic minerals (e.g., olivine) and possible loss of Mg associated with small degrees of dissolution that may have already occurred in our protolith sample. The slightly high Al_2O_3 content of the protolith also suggests that the protolith may have already experienced some weathering.

The major element concentrations of the soil samples are very different from our relatively unweathered bedrock protolith and suggest extensive weathering (Fig. 2). The SiO_2 concentrations in the bedrock range from 3 to 4 wt.% below 200 cm and from 17 to 22% above 200 cm, indicating extensive Si dissolution in all parts of the soil column. Si loss appears to be greatest in the deepest section of the soil profile. The elements, Na, K, Ca, and Mg, all of which are relatively mobile like Si, have also been lost from the soil to varying degrees, and like Si, appears to be most depleted from the lower layer. The zonations in Si, Na, K, Ca, and Mg contents suggest that the lower layer is more developed. This is consistent with Zr, Hf, Nb, and Ta concentrations, which increase with depth by more than a factor of two. As we will
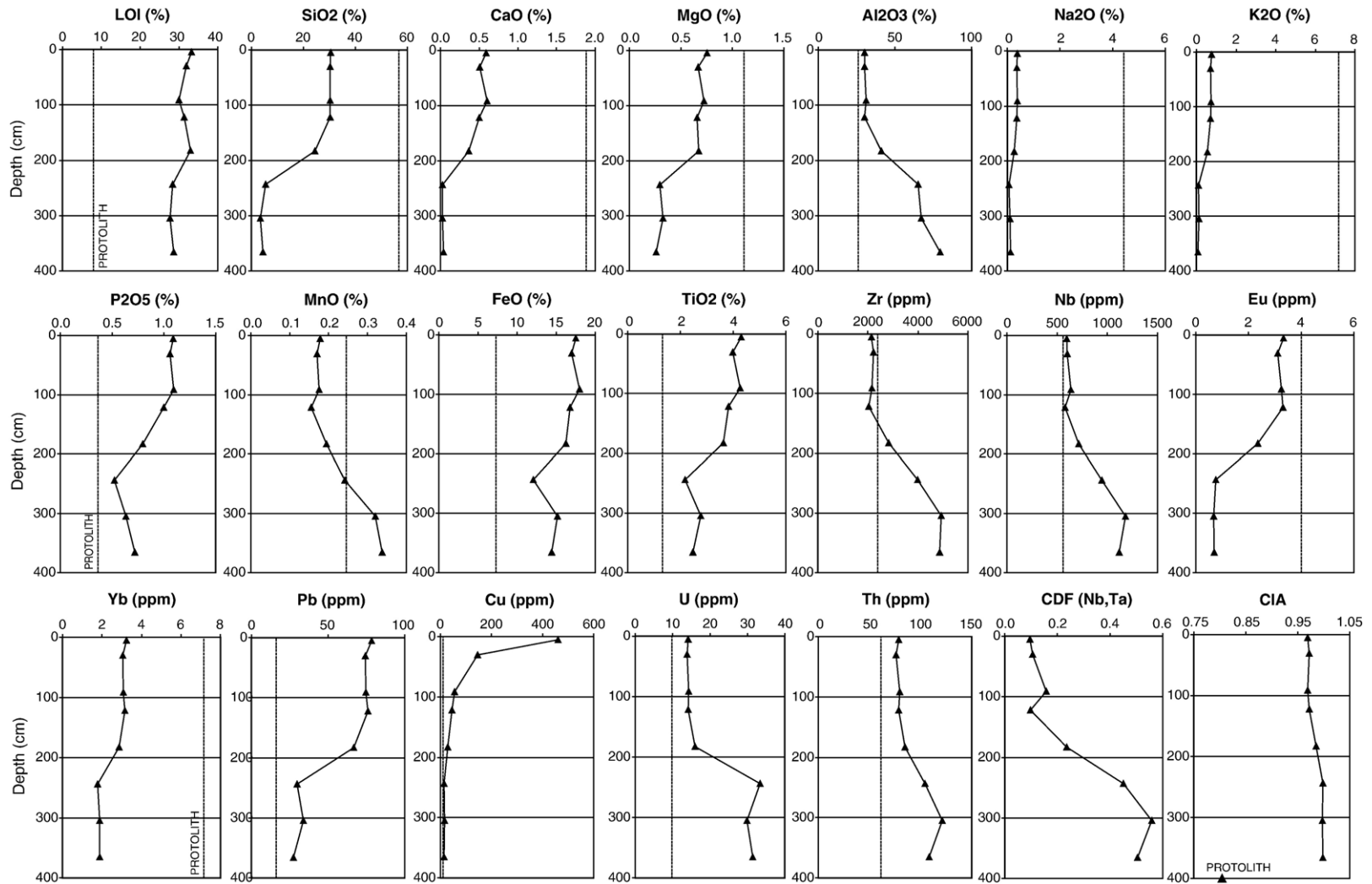
Fig. 2. The loss on ignition (LOI), LOI-corrected element concentrations (SiO$_2$, CaO, MgO, Al$_2$O$_3$, Na$_2$O, K$_2$O, FeO, TiO2, Zr, Hf, Ta, Nb, Yb, Pb, Cu, U, and Th), Chemical Depletion Factor (CDF), and Chemical Index of Alteration (CIA) are plotted by depth. Also plotted as a dotted line or marked symbol are the LOI, element concentrations, and CIA of the protolith. The Chemical Index of Alteration is defined as CIA $= \frac{Al_2O_3}{Al_2O_3+CaO+Na_2O}$ (Nesbitt and Young, 1984). The Chemical Depletion Factor is averaged for Nb and Ta, where CDF $= 1-\frac{X_{rock}}{X_{soil}}$ (Riebe et al., 2003).

discuss in more detail in Section 5.2, these elements are relatively immobile, hence their concentrations should increase with progressive weathering dissolution. We note that two other elements often used as immobile element tracers, Al and Ti, may have been mobilized as the LOI-corrected Al and Ti contents are higher than the protolith throughout the soil column (Fig. 2).

The rare earth elements (REEs) also display some consistent patterns (Fig. 3). Except for Ce, REE concentrations are slightly depleted (relative to the protolith) throughout the soil column, being most depleted at depths greater than 200 cm. The depletion of REEs appears also to be accompanied by subtle fractionations in the relative abundances of the REEs. A

positive Ce anomaly (relative to the other REEs) has developed throughout the soil column. In some cases, the Ce concentrations are enriched over the protolith and in some cases depleted, but there is no apparent systematic correlation with depth unlike the gross behaviors of the other REEs. We also note that above 200 cm, the protolith-normalized abundance patterns are convex upwards and show subtle positive Eu anomalies (relative to the other REEs). The convex REE profiles suggest at face value that the light REEs and heavy REEs may have been more efficiently depleted than the middle REEs. At depths greater than 200 cm, the protolith-normalized abundance patterns are remarkably flat (i.e. no Eu anomaly) except for the positive Ce anomaly.
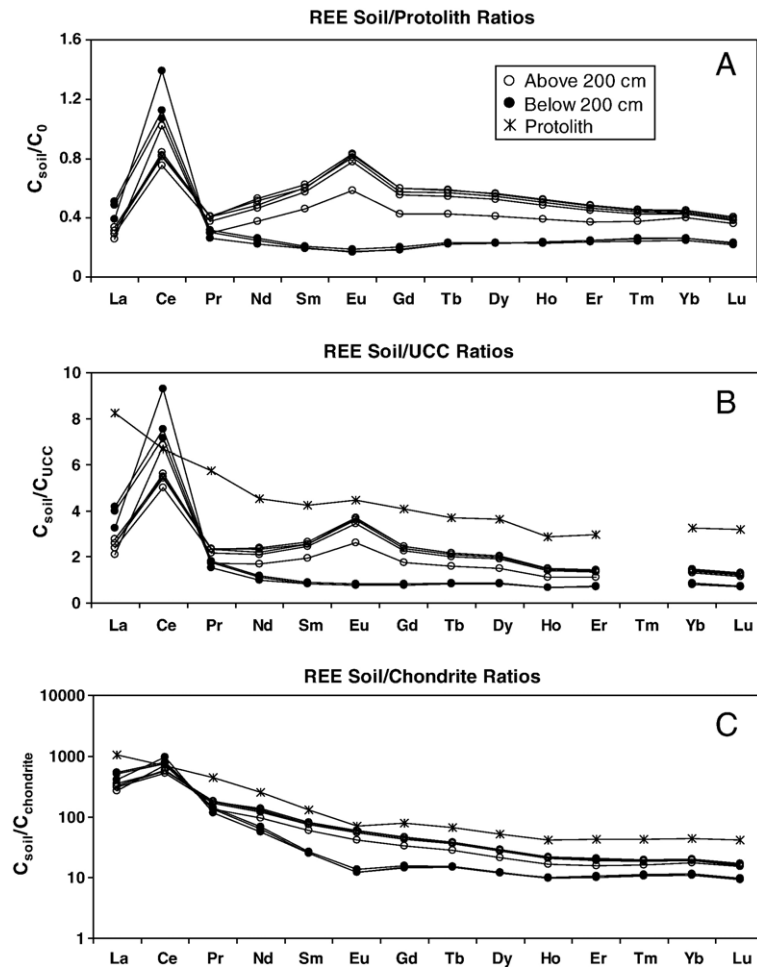
3

Fig. 3. Here we present three plots of REE concentration ratios (La, Ce, Pr, Nd, Sm, Eu, Tb, Gd, Dy, Ho, Er, Tm, Yb, and Lu). Soil/protolith REE concentrations are plotted for plotted samples above 200 cm (○), and samples below 200 cm (●) in ppm in [A]. Also plotted are soil/upper continental crust [B] and soil/chondrite [C] concentration ratios for the REE's. In [B] and [C], ratios are also plotted for the protolith sample as (*).

Finally, one suite of elements shows clear surface enrichments. The major element oxides P_2O_5 and TiO_2 have been enriched from ~ 0.4 to 1% and ~ 1 to 4%, respectively, from the protolith to surface layer. Co, Pb, Cu, Cr, Ni, and V show much larger surface enrichments: at the surface these elements may be 2 orders of magnitude greater than concentrations in the protolith and at depth (Fig. 2). U and Th show moderate enrichments throughout the soil column though the enrichments below 200 cm are greatest (Fig. 2).

5. Estimating mass changes during soil formation

The elements Zr, Hf, Nb, and Ta are generally considered immobile (conservative), hence their weight concentrations should increase with increasing degree of mass dissolution associated with weathering. In most soil profiles, it is the shallowest parts that have been undergoing weathering for the longest times, thus the concentrations of immobile elements should be elevated at shallow levels, gradually decreasing with depth down to the bedrock. However, the Machame soils are enriched in Zr, Hf, Nb, and Ta at depth (Fig. 2). In this section, we attempt to quantify the amount of dissolution experienced in the soil column. In Section 6, we discuss possible mechanisms for the formation of an apparent inverted soil profile.

5.1. Calculating chemical weathering and element mobility

The Chemical Depletion Factor (CDF) and the Chemical Index of Alteration (CIA) are two proxies for chemical weathering (Nesbitt and Young, 1984; Riebe et al., 2003). The CDF is an estimate of mass changes during soil formation based on immobile elements where,

$$CDF = 1 - \frac{C^i_{rock}}{C^i_{soil}} \tag{1}$$

The CDF is an approximation of the fraction of net mass removed during soil formation so that values approach zero for the least weathered soil and values approach 1 for highly weathered soils. The CIA is an estimate of the amount of chemical weathering based on the ratio of Al, which is relatively refractory, to the sum of Al and more mobile major elements Ca and Na where,

$$CIA = \frac{Al_2O_3}{Al_2O_3 + CaO + Na_2O} \tag{2}$$

As a rock is weathered and the Ca and Na are preferentially dissolved, the CIA increases from initial

values of around 0.6 for upper continental crustal rocks to a maximum of 1.0. These two proxies provide a generic method of comparison to other soils and within the profile.

We also want to determine the mobility of individual elements. To do this we estimate relative mass losses and additions by considering a mass balance approach, that is,

$$M_0 = M_{soil} + M_\Delta$$

$$m_0 = m_{soil} + m_\Delta \tag{3}$$

where M_0 represents the total mass of the original parent material, M_{soil} is the mass remaining in the soil residue, M_Δ is the net mass change during weathering by such processes as chemical weathering, aeolian deposition, or authigenic precipitation from solute-laden water derived from other parts of the weathering profile or precipitation (Brimhall and Dietrich, 1987). The lowercase m_0 represents the mass of one element in the original parent material, m_{soil} is the element in the soil, and m_Δ is the net mass change of that element during weathering. We explicitly ignore the effects of adding water or organics; therefore, all concentrations referred to herein are LOI-corrected. Before we can estimate the relative amount of each element lost, we must first identify the relationship between the mass of the original protolith, the mass of the soil produced, and the concentrations of immobile elements in the protolith and the soil. The mass ratio of original protolith to current soil can be estimated by,

$$\frac{M_{soil}}{M_0} = \frac{C^i_0}{C^i_{soil}} \tag{4}$$

where C^i_0 is the weight concentration of an immobile element i in the original bedrock protolith and C^i_{soil} is the concentration of the same immobile element in the soil. It follows that the ratio of the mass change of a mobile element, j, to mass of that element in the protolith can be expressed by,

$$\frac{m^j_\Delta}{m^j_0} = \frac{\frac{C^i_0}{C^i_{soil}} * C^j_{soil} - C^j_0}{C^j_0} \tag{5}$$

This equation allows us to estimate the relative change in mass of a particular element lost or gained.

5.2. Identification of an appropriate immobile element tracer

The first step in estimating mass losses and additions is to correct measured elemental concentrations in the dry

soil and bedrock for volatiles, such as organic carbon and water. The correction factor is determined from the loss on ignition (LOI in Table 1), which is a measure of how much organic carbon, water and other volatiles present in the soil but not likely to be derived from the protolith itself. The second step is to identify an appropriate immobile element tracer. In reality, no elements exhibit true immobility; however, there are a few that have been proven to be relatively immobile. Ti and Al are often treated as immobile elements during various weathering processes (Colman, 1982; Cramer and Nesbitt, 1983; April et al., 1986; Middelburg et al., 1988; Gouveia et al., 1993; Taylor and Blum, 1995; Teutsch et al., 1999; Sak et al., 2003). Their popularity is largely due to the fact that measurements of Ti and Al are routine. However, elements such as Zr, Nb and Ta have also been used (Brimhall et al., 1988, 1991; Kirkwood and Nesbitt, 1991; Bain et al., 1993; Kurtz et al., 2000). What all of these elements have in common is that they are relatively high field strength elements (ionic charge/ionic radius) and hence have limited solubilities in water. The question is which one of these elements is likely to be the least mobile. Al is actually the most mobile of these elements, consistent with its lower field strength compared to Zr, Ti, Nb and Ta (Vitousek et al., 1997). Nevertheless, Ti has also been shown to be mobile (Brimhall et al., 1988). Under conditions of Ti and Al mobility, it has been suggested that Nb and Ta may remain relatively immobile (Kurtz et al., 2000).

We can assess the behaviors of Nb, Ta, Zr, Hf, Al, and Ti in the Machame soils. An additional element, Hf, is considered because of its similar geochemical behavior to Zr. Table 3 presents the protolith to soil concentration ratios, $\frac{C_0^i}{C_{\text{soil}}^i}$, of Nb, Ta, Zr, Hf, Ti, and Al. The values calculated from Nb, Ta, Zr, Hf, and Al suggest a spectrum

Table 3
Protolith to soil ratios, C_0/C_{soil}, for Ti, Al, Zr, Hf, Nb, and Ta

C_0/C_{soil}	5 cm	30	91	122	183	244	305	366	Protolith
Ti	0.30	0.33	0.31	0.34	0.36	0.60	0.47	0.53	
Al	0.86	0.86	0.83	0.86	0.63	0.40	0.39	0.33	
Zr	1.12	1.07	1.10	1.18	0.84	0.60	0.48	0.49	
Hf	1.02	1.05	1.04	1.03	0.81	0.53	0.46	0.52	
Nb	0.94	0.93	0.88	0.96	0.78	0.59	0.47	0.50	
Ta	0.87	0.86	0.80	0.84	0.75	0.51	0.41	0.49	
CIA[a]	0.97	0.97	0.97	0.97	0.98	1.00	1.00	1.00	0.80
CDF[b]	0.10	0.11	0.16	0.10	0.24	0.45	0.56	0.50	

All data corrected for LOI.
[a] Chemical Index of Alteration, where CIA = $\frac{Al_2O_3}{Al_2O_3 + CaO + Na_2O}$ (Nesbitt and Young, 1984).
[b] Chemical Depletion Factor averaged for Nb and Ta, where CDF = $1 - \frac{X_{\text{rock}}}{X_{\text{soil}}}$ (Riebe et al., 2003).

of modest net mass change (+/−20%) above 150 cm depth and large losses (>40%) between below 150 cm (Ti is a distinct outlier because the $\frac{C_0^{\text{Ti}}}{C_{\text{soil}}^{\text{Ti}}}$ values suggest 70–75% mass removal above 150 cm). We can examine the geochemical behavior of these elements in detail by plotting Ta versus Nb, Hf versus Zr, Al_2O_3 versus Nb, and TiO_2 versus Nb in Fig. 4. Also plotted is the protolith reference line corresponding to the Ta/Nb, Hf/Zr, Al_2O_3/Nb, and Ti/Nb ratios of the protolith sample. Perfectly immobile elements should plot on the dotted line because while the absolute concentrations of two immobile elements will change due to dilution or concentration effects, their relative abundances should not. It can be seen from Fig. 5A and B that Nb/Ta and Zr/Hf ratios are remarkably constant as evidenced by the fact that the data points fall close to the protolith reference line. This suggests that Nb, Ta, Zr, and Hf are behaving as immobile elements. In contrast, the Al/Nb ratios of the most weathered samples deviate from the protolith reference line (Fig. 4C). This suggests that Al may have been added since Nb has now been demonstrated to be immobile. We also note that Ti /Nb ratios also deviate from the protolith reference line for samples above 200 cm, indicating that Ti has been added (Fig. 4D). Collectively, these observations suggest that Nb, Ta, Zr, and Hf are relatively immobile whereas Al and Ti are not. We note, however, that the apparent immobility of Zr and Hf may be partly coincidental. The LOI-corrected Zr and Hf concentrations appear to be slightly depleted (by about 10%) relative to the protolith, which suggests that Zr and Hf may have actually suffered small losses (Fig. 5). These observations are consistent with other observations that have shown that Zr (and by inference Hf) may be slightly mobile under intense weathering conditions. For example, during bauxite formation on volcanic rocks in Southern Brazil, Zr has been shown to be more mobile than Fe and Nb using isovolumetric mass balance methods (Melfi et al., 1996). In all ensuing discussions, we have thus chosen Nb and Ta as our most immobile element tracers.

5.3. Estimating mass fluxes

Nb and Ta concentrations are used in conjunction with Eq. (3) to estimate the total amount of original protolith mass remaining in the soil residuum. If there has been significant mass loss, the mass concentrations of Nb and Ta (corrected for LOI) should be greater than that of the protolith. It can be seen from Fig. 4 that the LOI-corrected Nb and Ta concentrations are slightly higher (10%) than that of the protolith in the upper 200 cm of the weathering profile and significantly higher (200%) in the lower 200 cm. These features
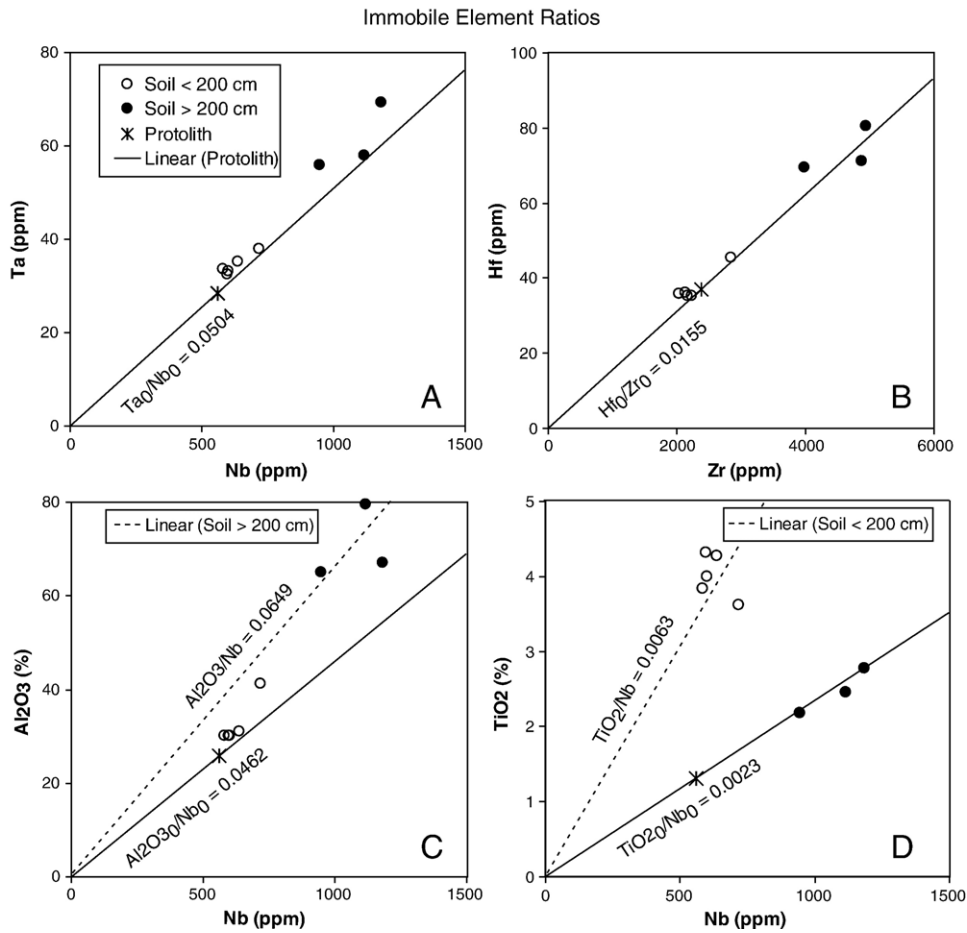
Fig. 4. Highly refractive elements that are commonly used for mass balance calculations are plotted against each other. Concentrations of Ta v. Nb [A], Hf v. Zr [B], Al_2O_3 v. Nb [C], and TiO_2 v. Nb [D] plotted for bedrock (*), samples above 200 cm (○), and samples below 200 cm (●) in ppm. The dotted line from the origin through the bedrock data is the evolution path available to ideal, immobile elements. Samples that plot upslope from the bedrock datum have a net mass loss; samples that plot downslope from the bedrock datum have a net mass gain. The slopes of each solid origin-protolith line and the squares of the correlation coefficients (r^2) between each line and the soil sample data are reported. The dotted lines represent a linear best fit for the data above 200 cm in [C] and below 200 cm in [D] for comparison to the other data.

indicate that there has been mass loss throughout the weathering profile, with most of the loss occurring in the lower half of the profile. What is peculiar is that the LOI-corrected SiO_2 contents in the upper 200 cm appear to be substantially less than that of the protolith, implying that much greater amounts of dissolution may have occurred than implied from Nb and Ta concentrations in the upper 200 cm. There are three possible explanations for this. The first is that there may have been mass addition in the upper 200 cm, which dilutes the concentration of an immobile element. The second is that our presumably unweathered protolith, as pointed out in the Results section, has probably already undergone some amount of dissolution, which unfortunately we cannot quantify if a truly pristine protolith is unavailable. The third is that the soil protolith is not

homogenous with depth. The first two scenarios imply that our estimates of mass dissolution using Nb and Ta as immobile element tracers are probably minimum estimates. All of these scenarios will be discussed in greater detail in Section 6. For the remainder of Section 5, we will assume a homogenous protolith.

In Table 1 and in Fig. 2, we report the CIA and the CDF for each soil sample. The CIA factors are very close to unity throughout the column indicating a high level of weathering. Even the protolith sample, which we admitted was partially weathered, is 0.80, typical of a weathered bedrock sample. However, there is a discernable difference between the samples above 183 cm, which have a CIA of 0.97, and those below which have a CIA of 1.00. The CIA of the soil sample at 183 cm is 0.98, closer to the more shallow samples than
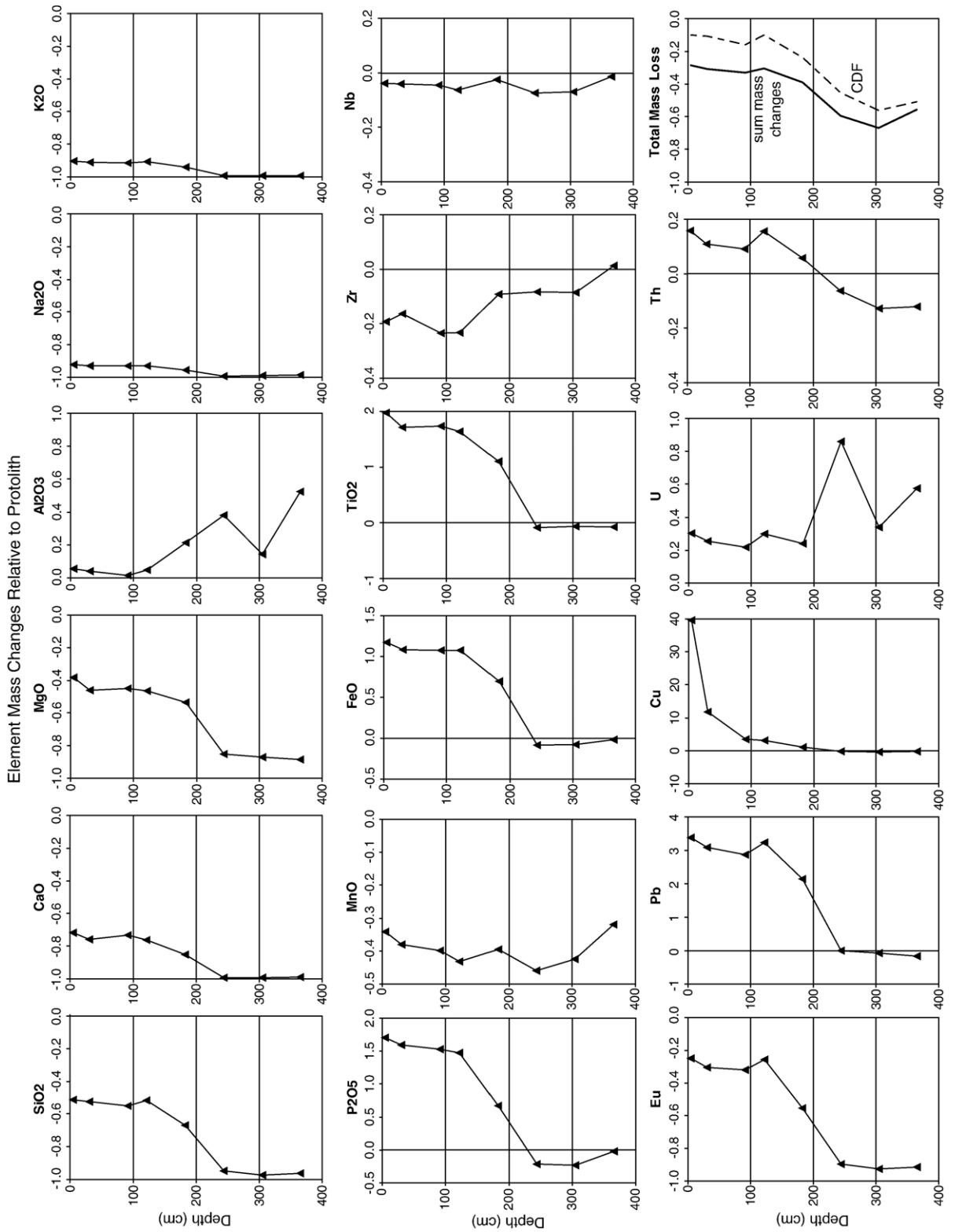
the deeper ones; however, it may also represent a transition from less to more weathered material. The CDF, an estimate of net mass loss, indicates that the orginal protolith underwent a net ∼10% loss of mass above 183 cm and a net loss of ∼50% below 183 cm. The soil sample at 183 cm again shows an intermediate net loss of ∼25%. The CIA and CDF both indicate that weathering throughout the soil column increases with depth.

Our mass balance calculations can be extended to estimating the mass dissolution flux of each element. Fig. 5 is a plot of $\frac{m_D^j}{m_0^j}$ for the major elements, SiO$_2$, CaO, MgO, Al$_2$O$_3$, Na$_2$O, P$_2$O$_5$, MnO, FeO, K$_2$O, and TiO$_2$ and the trace elements Zr, Nb, Eu, Pb, Cu, U, and Th calculated from Eq. (5). These values generally represent time-averaged losses during pedogenesis that contribute to the dissolved load that eventually makes it to the rivers. Given their weight percentages in the bulk rock, it is clear from Fig. 5 that the time-averaged dissolution flux should be dominated by Si, K, and Na. Interestingly, there appears to be a net addition of Fe in the upper 200 cm and a net addition of Al below 200 cm, suggesting that Fe and Al and have either been redistributed in the soil column or that excess Fe and Al has been introduced from outside of the soil system. Ti, Fe, and P exhibit somewhat unusual behaviors in that they are all added above 200 cm but relatively immobile below. Al is the only major element significantly added below 200 cm. The last panel in Fig. 5 shows a sum of all of the major and minor element losses throughout the soil column as well as the Chemical Depletion Factor. While there is a discrepancy between the two estimates of total mass loss, they are well correlated and the absolute deviation between the estimated decreases with depth.

6. Possible explanations for the inverted weathering profile

The CIA, Table 1 and Fig. 2, and the relative mass losses, $\frac{m_D^j}{m_0^j}$, in Fig. 5 show that there have been huge mass losses throughout the soil column with the more depleted layers occurring below 200 cm. There are at least four hypotheses that may explain some parts or all of this phenomenon. Before we explore these hypotheses, we rule out from the outset the possibility that lateral movement of material through colluvial processes and landslides has led to the development of these

geochemically stratified zones. Below, 200 cm, the soil is extremely weathered, but possesses a rigid, highly pourous structure which would most likely be destroyed with significant lateral movement of solid material. The horizons above 200 cm appeared to be laterally homogenous and without large clasts both of which suggest that any recent contribution to the soil from colluvial processes is limited and insignificant.

We must also mention the surface enrichments of Pb, Cu, and P which remain unexplained by the four natural, non-anthropic hypotheses presented below. There is a wealth of research documenting the surface enrichment of Pb, Cu and other metals through anthropogenic deposition and biocycling (Olson and Skogerboe, 1975; Hamelin et al., 1989; Alloway, 1995; Han and Banin, 1997; Keller and Domergue, 1996; Erel et al., 1997; Othman et al., 1997; Wilkens and Loch, 1998; Lee et al., 1998; Hansmann and Koppel, 2000; Blaser et al., 2000; Teutsch et al., 2001; Wilcke et al., 2001; Halamic et al., 2003). In agricultural settings, fertilization and manure application can lead to persistant P enrichments (Carpenter et al., 1998). While atmospheric dust cannot account for Pb, P, and Cu, exclusively, other anthropic depositions such as fertilizer, manure, and particulates from exhaust and smoke could account for surface enrichments of these elements.

We now proceed to lay out each of the four hypotheses and explore their plausibilities in the context of the data.

6.1. Re-precipitation followed by erosion

One way to achieve higher concentrations of certain major elements at the surface is to invoke recent erosion (Fig. 6A). This scenario could work as follows. The first step is the development of a deep, mature soil profile from the top–down. Soluble elements such as Ca, Sr, Na, and Mg would be leached throughout the soil column with the upper parts experiencing greater depletion. Fe and other particle reactive elements, such as Mn and Mg, leached from the upper part of the soil column, will migrate downward and reprecipitate onto clay surfaces and/or form amorphous Fe and Mn hydroxides, generating an enrichment front just beneath the depleted upper layer. If the upper horizons above the enriched layer are subsequently removed through rapid physical erosion (by rapid, we mean faster than the

Fig. 5. The relative mass change, $\frac{m_D^j}{m_0^j}$, is plotted for SiO$_2$, CaO, MgO, Al$_2$O$_3$, Na$_2$O, K$_2$O, P$_2$O$_5$, MnO, FeO, TiO$_2$, Zr, Nb, Eu, Pb, Cu, U, and Th from Eq. (5). Also plotted are two estimates of the total mass loss during pedogenesis. The solid line is the sum of all mass differences calculated using Eq. (5), $\sum m_D^j = \sum \frac{C_0^i}{C_{soil}^i} T C_{soil}^j - C_0^j$, and the dashed line is the Chemical Depletion Factor (CDF). Discrepancies between these two lines represent measured mass losses unaccounted for by the immobile element ratios.
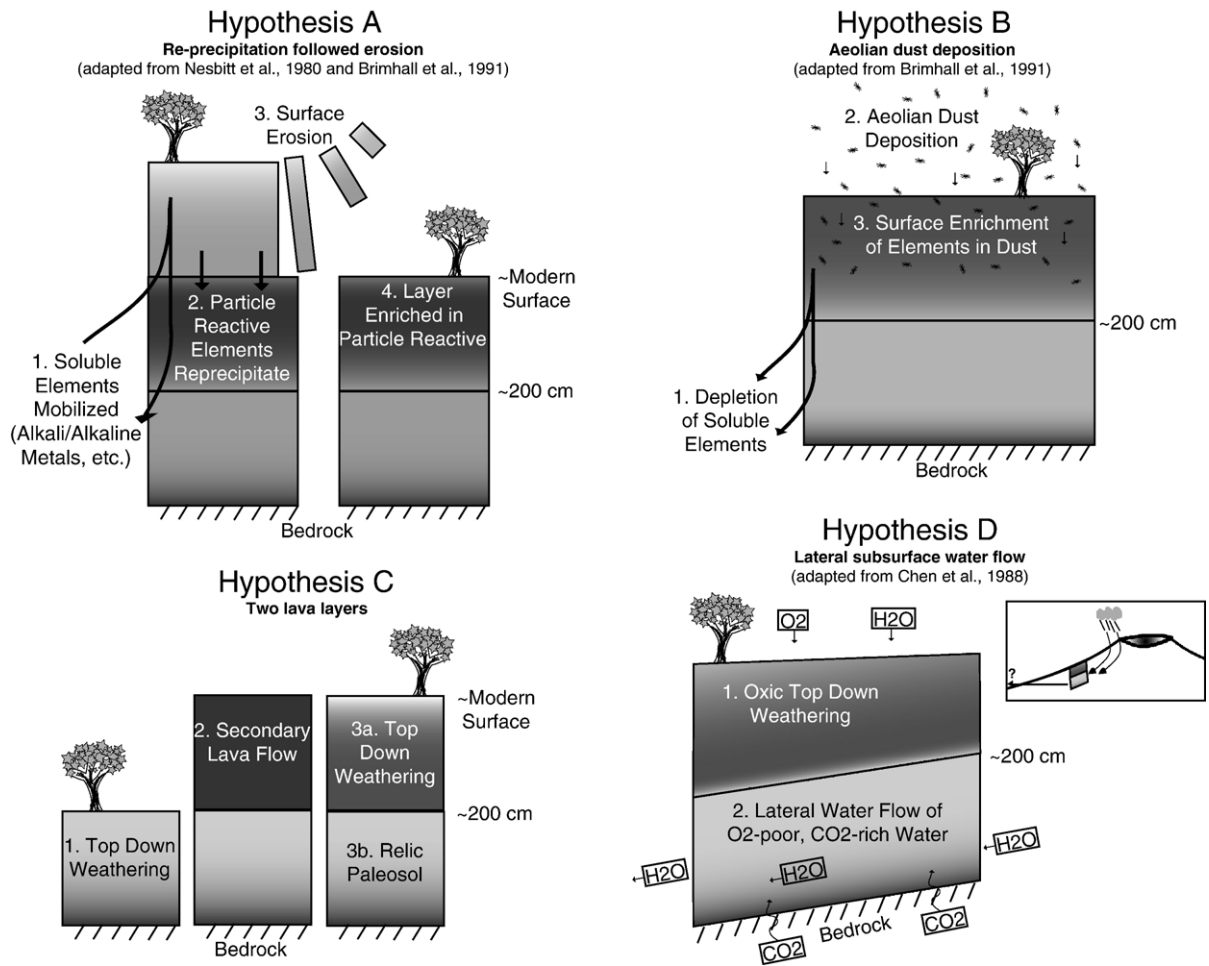
Fig. 6. Schematic models of four hypotheses to explain the formation of the Machame soil profile. Hypotheses A describes re-precipitation of particle reactive elements followed by latter-day surface erosion. Hypothesis B requires the addition of many elements by Aeolian dust deposition. Hypothesis C proposes that the soil was formed from two different lava layers. Hypothesis D calls for enhanced weathering due to lateral subsurface water flow. We have also included an inset for the subsurface flow model that shows a potential recharge mechanism.

timescales of leaching and downward migration and re-precipitation of particle reactive elements), the enriched layer could be exposed at the surface, giving the artifact of an inverted soil profile. In other words, this hypothesis would require the upper 200 cm of our soil profile to represent a paleo-enrichment front (Nesbitt et al., 1980).

Re-precipitation may be able to explain the Fe added above 200 cm in the Machame profile (Fig. 5) and may also explain Ti which has a concentration profile (Fig. 2) and relative mass loss profile (Fig. 5) very similar to the respective profiles of Fe. Like Fe, Ti has been shown to be mobile in highly weathered tropical environments (Cornu et al., 1999). Cornu et al. (1999) showed significant Ti losses through the formation of anatase precipitates as well as general mobility due to plant–soil cycling. Some re-precipitation processes may also

explain the slight Th enrichments observed in the upper 200 cm (Fig. 5) as Th may be mobilized in association with dissolved organic matter or colloids in some marine environments (Guo et al., 1997). Th was found to be mobilized through dissolution/re-precipitation processes or association with organic colloids in a tropical watershed in Cameroon (Braun et al., 2005). The presence of colloids, organic matter, and water provide the conditions necessary for the mobilization of Th. Therefore, the enrichment of Fe, Ti, and Th in a zone of reprecipitation may be feasible.

Despite these successes, the model simply fails to explain the majority of the major elements. Ca, Mg, Na, K, and Si are not particle reactive; hence, their higher abundances in the upper 200 cm cannot be explained by this same process. This process is thus considered untenable in explaining the inverted soil profile.

6.2. Aeolian dust deposition

Atmospheric dust deposition is another hypothetical mechanism that might be invoked to explain high elemental concentrations above 200 cm relative to concentrations below 200 cm (Fig. 6B). Dust deposition has been suggested to explain the development of some bauxite formations which, like the Machame soils, have high Al_2O_3 contents (Brimhall et al., 1988). Marine aerosol deposition has also been shown to be critical to soil formation and maintaining nutrient budgets on the Hawaiian Islands (Chadwick et al., 1999). At more than 250 km from the Indian Ocean, it is doubtful that marine aerosols have a significant impact on soils in Mt. Meru; thus, we will restrict our discussion to continentally derived dust. For the Machame region, the dust deposition hypothesis requires that dust is deposited at the surface of the soil column. The dust must then be mixed down into the soil column by burrowing animals, roots, clay shrink/swell, and/or other biological and physical processes (Brimhall et al., 1991). The dust may originate locally or be blown in from great distances (Chadwick et al., 1999; Grousset and Biscaye, 2005). As a result, enrichments in atmospherically deposited elements are superimposed onto a mature soil profile. A closer look at what elements are enriched and the nature of their enrichments can help to assess the plausibility of this scenario in explaining our apparent inverted soil profile.

Firstly, the profiles of the major elements do not seem to be consistent with surface deposition. Ca, Mg, Si, Pb, P, Fe, and Ti are enriched at the surface but abruptly decay in concentration below 122 cm. If these surface enrichments are associated with external (Aeolian) inputs, then we would expect the downward depth distribution of these elements to decay monotonically with depth due to downward transport by bioturbation (Brimhall et al., 1991). The step function stop in concentration of the above-mentioned elements is inconsistent with an external surface input. The only element to show a monotonic decay with depth is Cu.

The applicability of the Aeolian hypothesis can be further assessed by examining the magnitude and composition of the elemental enrichments at the surface. If the surface enrichments above ∼200 cm are caused by dust inputs, we can take the composition of the soil below 200 cm to be the baseline composition of the profile. We can then estimate a *minimum* percentage of the soil column that originated as dust by summing all elemental mass enrichments above the baseline concentrations. We find that at least 38% of the total soil dry mass down to 200 cm must be dust-derived in order to account for the concentration profiles of the major elements. We can also calculate the chemical composition of the dust which results in the following major element composition: 66% SiO_2, 23% FeO, 7% TiO_2, 2% K_2O, 1% MgO, 1% CaO, 1% Na_2O, and 0% Al_2O_3. Dust of this composition most likely represents a mixture of quartz, iron oxides (magnetite, spinel), and Ti-bearing oxides (rutile and ilmenite), implying an origin from felsic continental crust. Such material would be expected to be enriched in the high field strength elements due to the presence of Ti-bearing oxides (which could be used to explain the high Ti in the upper layer). If this material was a significant component of the upper layer of the Machame soil profile, the high field strength element systematics would be controlled to a large extent by the dust. This dust, however, would be characterized by low Nb/Ta ratios. This is because the source of this dust, upper continental crust, typically has Nb/Ta ratios between 10–12 (Rudnick and Fountain, 1995), much lower than most intraplate volcanic rocks, such as our Machame protolith. In fact, the hypothetical dust should have even lower Nb/Ta ratios because it is known that rutile, the dominant repository for Nb and Ta in silicate rocks, prefers Ta over Nb and hence typically has a low Nb/Ta ratio compared to the host rock (Klemme et al., 2004). The fact that the Nb/Ta ratios of the Machame soils are high (∼20, a typical value for mantle-derived rocks) and *constant* throughout the soil column implies that dust of the required composition did not fall in amounts sufficient to generate the enrichments seen in the upper layer. Furthermore from Fig. 3C, it is clear that the soil/chondrite REE ratios for the *shallow* Machame soils do not exhibit the behavior expected with a significant contribution of continental crust because there is no negative Eu anomaly as well as high soil/chondrite ratios (Kurtz et al., 2001). Thus, dust deposition cannot adequately reconcile the major and trace element data and is therefore an unreasonable hypothesis to explain the inverted profile.

6.3. Buried Paleosol

The two chemically distinct soil layers may represent two soils of different ages formed from two different lava flows (Fig. 6C). In this scenario, a soil, now represented as the Machame soil below 200 cm, formed on a lava flow-chemically identical to the material that we sampled as the Machame protolith. After this soil develops and is extensively weathered, it is covered by a subsequent lava flow. The overlying lava flow then undergoes weathering itself and forms a second soil horizon, now represented as the soil above 200 cm.

Assuming similar weathering rates for the development of the relic soil and the modern soil and given the significantly more depleted horizons below 200 cm, this model requires that the relic soil was directly exposed to the atmosphere much longer than the modern soil has been.

This model could, in theory, explain why the upper layer is less weathered than the deeper layer. It can also explain the behavior of Eu relative to the other REE's. The Machame protolith is rich in plagioclase phenocrysts. These plagioclase phenocrysts have preferentially partitioned Eu into their mineral lattices over other REEs, a process which left the complementary glassy matrix poor in Eu. Because glass lacks crystalline structure, the glassy matrix is more susceptible to chemical weathering than the plagioclase phenocrysts. According to this two lava hypothesis, the relic soil below 200 cm was weathered more intensely, destroying nearly all primary minerals, including plagioclase. This would explain the positive Eu anomaly above 200 cm and lack of an anomaly below 200 cm (Fig. 2).

Some characteristics of the soil, however, are inconsistent with a buried paleosol model. First, the soil profile lacks physical evidence of a bake zone in the field. If the soil below 200 cm did represent an older relic soil, we would expect a bake zone to be found between the soils. This bake zone would have probably been highly resistant to weathering and should have been preserved. Second, the depth behavior of chemical weathering, manifest in terms of CIA and CDF, is inconsistent with a buried paleosol. If the change in composition at ∼200 cm indeed represents a transition from a younger, less weathered soil and to an older paleosol, we would expect to see a decrease in the degree of weathering as we approach this boundary from above. Conversely, as we approach the transition from below, we would expect to observe an *increase* in the degree of weathering. The constant weathering degrees in the upper and lower layers may be inconsistent with this hypothesis. However, the buried paleosol model is consistent with the bulk of the geochemical data including Al and is, therefore, a viable mechanism for soil formation in the Machame region.

6.4. Lateral subsurface water flow

A fourth hypothesis involves enhanced weathering due to lateral subsurface water flow, (Fig. 6D). Meteoric waters enter the subsurface at higher elevations. This subsurface water then flows from its recharge region down the flanks of the mountain, the flow being driven by the hydraulic head imposed by mountain topography. This model yields

the following predictions. Progressive reaction of a package of groundwater along its flow path should lead to 1) consumption of oxygen due to oxidative weathering (i.e., $0.5O_2 + 2FeO = Fe_2O_3$) and 2) consumption of CO_2 due to acidic breakdown of silicate (e.g., $CO_2 + H_2O + CaSiO_3 = HCO_3^- + Ca^{2+} + HCO_3^-$). As such, we might expect weathering by subsurface water flows to be large only near recharge point but small further along the flowpath. However, in volcanically active regions, there is likely a constant background flux of volcanic gasses permeating through the volcano (Cruz et al., 1999; Aiuppa et al., 2000). Such gases will be reducing but rich in CO_2, and as a consequence, flux of such gasses into the subsurface water could increase acidity but not lead to an increase in O_2. Thus, in volcanically active regions, we might expect subsurface groundwater to be acidic and reducing.

If this model is applicable to our study site, the implication is that the entire soil profile has formed from the same protolith as a result of stratification in weathering processes. The soil above 200 cm was formed from typical top–down weathering while the soil below 200 cm was created contemporaneously by subsurface water flow, the two weathering regimes being distinguished by their different weathering rates (below 200 cm is faster) and possibly by different redox conditions. The former is suggested by the step function distribution of Ca, Mg, Na, and Si (Fig. 2) and the shallow Eu anamoly (Fig. 3A). The latter is suggested by the contrasting behaviors of U and Th in the two layers (Fig. 7). Th appears to be enriched in the upper 200 cm (i.e., high Th/Nb) and depleted below 200 cm, indicating that Th is relatively immobile in the
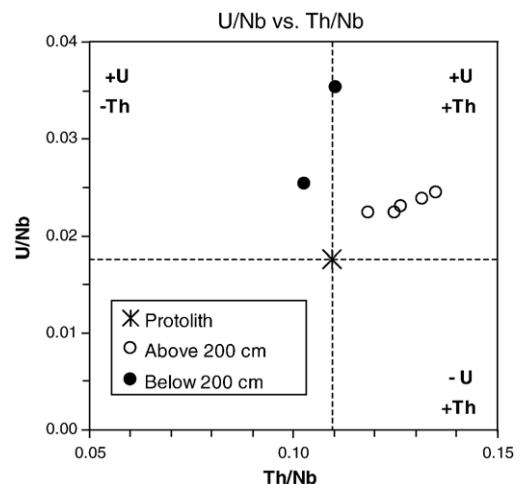

Fig. 7. U/Nb and Th/Nb ratios plotted for bedrock (∗), samples above 200 cm (○), and samples below 200 cm (●).

top layer but mobile in the bottom layer. U appears to be enriched relative to Nb at all depths, but the enrichment in U is greatest in the bottom layer. The U/Nb systematics indicate that U has been added at all depths, particularly in the bottom layer. These features suggest that the bottom layer may have been somewhat reducing and the top layer more oxidizing. This redox stratification would allow for Th mobility and preferential immobilization of U in the more reducing bottom layer and Th immobility and variable behavior of U in the more oxygenated upper layer (Langmuir, 1997). Focused subsurface water flowing through the bottom layer would be consistent with these observations. In fact, the net additions of U throughout the soil column, particularly in the bottom layer, are probably not solely sustainable by leaching of U from the surface followed by re-precipitation at depth. In this model, net additions of U are due to immobilization of dissolved U in subsurface water being laterally advected through the system. The upper 200 cm corresponds to the unsaturated vadose zone, which would be relatively oxygenated. Therefore, the subsurface flow model is consistent with the major and trace geochemical data, except Al, and with the physical data and thus remains a viable hypothesis to explain the formation of the Machame soils.

7. Implications of lateral subsurface water flow

Based on our discussion in Section 6, the data appear to be best explained by the buried paleosol scenario or the subsurface water flow model-with the caveat that Fe and Ti behavior may be the result of mobility due to re-precipitation or association with colloids. While we cannot confidently rule out either hypothesis, we believe that the subsurface water flow model deserves particular attention because it can explain the unusual U/Th systematics. If our bias is correct, there are some novel implications of lateral subsurface water flow. Our case study would suggest that groundwater weathering could increase local weathering rates by at least a factor of two (Table 3). This means that if only typical top–down soil formation processes are considered, weathering rates could be under-estimated. We note that the importance of subsurface water weathering may not be confined to our case study. Chen et al. (1988) concluded that bauxites in the Tatun volcanic region of northern Taiwan were also formed by enhanced weathering associated with groundwater flow (Chen et al., 1988). In south Asia, Basu et al. (2001) showed that groundwater may be as important as surface water from the Ganges–Brahmaputra river system in delivering dissolved Sr to the oceans (Basu et al., 2001).

Finally, Manga (1998) has shown that there is extensive groundwater flow in the Oregon Cascades arc (Manga, 1998). What all of these regions have in common is a large and steady recharge zone of meteoric water and a strong topographic gradient to drive groundwater flow. These regions are also subject to volcanic degassing or metamorphic decarbonation reactions.

If weathering by subsurface water flow turns out to be significant in volcanic or tectonically active regions, this phenomenon is not only important for soil formation and ocean trace element budgets, but possibly for the global carbon cycle. The weathering of silicate rocks is a slow, but permanent means of sequestering carbon (Berner et al., 1983). Our data suggest that weathering associated with subsurface water flow is 30% more effective than top–down soil formation processes at mobilizing Ca. For Mg, the subsurface water is 90% more effective at our site than top–down processes. It is possible that the enhanced weathering by subsurface water flow in our study site is facilitated by the addition of volcanic CO_2 slowly seeping out of the mountainside. Assuming that Ca and Mg are the primary cations responsible for silicate CO_2 sequestration, our study suggests that estimates of the CO_2 drawdown capacity of silicate weathering, at least in volcanically active regions, may need to account for weathering by subsurface water flow. If so, weathering by subsurface water flow may be a means of modulating the amount of CO_2 emitted from volcanic environments.

8. Conclusions

We investigated an inverted weathering profile formed on a volcanic substrate on the southern slopes of Mount Kilimanjaro, Tanzania, a region having a tropical equatorial climate. The following conclusions were made:

1) The degree of chemical weathering increases with depth into the soil profile.
2) The depletion of mobile major elements, Si, Na, K, Ca, and Mg, and the relative immobility of Al have created soils of 30–40 wt.% Al_2O_3 at depths greater than 200 cm.
3) The refractory elements Nb, Ta, Zr, and Hf are shown to be immobile throughout the soil column while Ti and Al are not. Ti and Fe are enriched above 200 cm and immobile below while Al appears to be slightly depleted at shallow depths but enriched at greater depths.
4) All geochemical and physical evidences suggest the presence of two distinct weathering regimes separated at 200 cm.

5) Two models can explain the bulk of the chemical and physical observations: either a buried paleosol or intense weathering associated with lateral subsurface water flow.

6) If subsurface water flow is responsible for the formation of the Machame soils, inputs of trace elements and Ca and Mg into the ocean budget are locally significant, and, if regionally representative, they should have implications for the global CO_2 cycle.

Acknowledgments

References

Aiuppa, A., et al., 2000. Mobility and fluxes of major, minor and trace metals during basalt weathering and groundwater transport at Mt. Etna volcano (Sicily). Geochimica et Cosmochimica Acta 64 (11), 1827–1841.

Alloway, B.J., 1995. Heavy Metals in Soils. Heavy Metals in Soils. Blackie Academic and Professional, Suffolk, England. 368 pp.

Anderson, G.D., 1982. A survey of the soils and land use potential of the southern and eastern slopes of Kilimanjaro, Tanzania. 1, Institute of Resource Assessment, University of Dar Es Salaam and International Development Program, Clark Univeristy, Dar Es Salaam.

April, R., Newton, R., Coles, L.T., 1986. Chemical weathering in the Adirondack watersheds: past and present-day rates. Geological Society of America Bulletin 97, 1232–1238.

Bain, D.C., Mellor, A., Robertson-Rintoul, M.S.E., Buckland, S.T., 1993. Variations in weathering processes and rates with time in a chronosequence of soils from Glen Feshie, Scotland. Geoderma 57, 275–293.

Basu, A.R., Jacobsen, S.B., Poreda, R.J., Dowling, C.B., Aggarwal, P.K., 2001. Large groundwater strontium flux to the oceans from the Bengal Basin and the marine strontium isotope record. Science 293, 1470–1473.

Berner, R.A., 1995. Chemical weathering and its effect on atmospheric CO_2 and climate. In: White, A.F., Brantley, S.L. (Eds.), Chemical Weathering Rates of Silicate Minerals. Reviews in Minealogy. Mineralogical Society of America, pp. 565–583.

Berner, R.A., Lasaga, A.C., Garrels, R.M., 1983. The carbonate–silicate geochemical cycle and its effects on atmospheric carbon dioxide and climate. American Journal of Science 283, 641–683.

Blaser, P., Zimmermanna, S., Lustera, J., Shotyk, W., 2000. Critical examination of trace element enrichments and depletions in soils: As, Cr, Cu, Ni, Pb, and Zn in Swiss forest soils. The Science of the Total Environment 249 (1–3), 257–280.

Braun, J.-J., et al., 2005. Present weathering rates in a humid tropical watershed: Nsimi, South Cameroon. Geochimica et Cosmochimica Acta 69 (2), 357–387.

Brimhall, G.H., Dietrich, W.E., 1987. Constitutive mass balance relations between chemical composition, volume, density, porosity, and strain in metasomatic hydrochemical systems; results on weathering and pedogenesis. Geochimica et Cosmochimica Acta 51 (3), 567–587.

Brimhall, G.H., et al., 1988. Metal enrichment in bauxites by deposition of chemically mature aeolian dust. Nature 333, 819–824.

Brimhall, G.H., et al., 1991. Deformational mass transport and invasive processes in soil evolution. Science 255, 695–702.

Carpenter, S., et al., 1998. Nonpoint pollution of surface waters with phosphorus and nitrogen. Ecological Applications 8 (3), 559–568.

Chadwick, O.A., Derry, L.A., Vitousek, P.M., Huebert, B.J., Hedin, L.O., 1999. Changing sources of nutrients during four million years of ecosystem development. Nature 397, 491–497.

Chen, C.-H., Liu, K.-K., Shieh, Y.-N., 1988. Geochemical and isotopic studies of bauxitization in the Tatun volcanic area, northern Taiwan. Chemical Geology 68, 41–56.

Colman, S.M., 1982. Chemical weathering of basalts and andesites: evidence from weathering rinds. USGS Professional Paper, vol. 1246.

Cornelius, D.J., 2004. Washington State University at Pullman's GeoAnalytical Lab. personal communication.

Cornu, S., et al., 1999. Evidence of titanium mobility in soil profiles, Manaus, central Amazonia. Geoderma 91 (3), 281–295.

Cramer, J.J., Nesbitt, H.W., 1983. Mass-balance relations and trace-element mobility during continental weathering of various igneous rocks. Sciences Géologiques. Mémoire 73, 63–73.

Cruz, J.V., Coutinho, R.M., Carvalho, M.R., Oskarsson, N., Gislason, S.R., 1999. Chemistry of waters from Furnas volcano, Sao Miguel, Azores: fluxes of volcanic carbon dioxide and leached material. Journal of Volcanology and Geothermal Research 92, 151–167.

Dawson, J.B., 1992. Neogene tectonics and volcanicity in the Noth Tanzania sector of the Gregory Rift Valley: contrasts with the Kenya sector. Tectonophysics 204, 81–92.

Dessert, C., et al., 2001. Erosion of Deccan Traps determined by river geochemistry: impact on the global climate and the $^{87}Sr/^{86}Sr$ ratio of seawater. Earth and Planetary Science Letters 188, 459–474.

Erel, Y., Veron, A., Halicz, L., 1997. Tracing the transport of anthropogenic lead in the atmosphere and in soils using isotopic ratios. Geochimica et Cosmochimica Acta 61 (21), 4495–4505.

Evernden, J.F., Curtis, G.H., 1965. The potassium–argon dating of Late Cenozoic rocks in Africa and Italy. Current Anthropology 6, 343–384.

Gaillardet, J., Dupre, B., Louvat, P., Allegre, C.J., 1999. Global silicate weathering and CO_2 consumption rates deduced from the chemistry of large rivers. Chemical Geology 159, 3–30.

Gouveia, M.A., et al., 1993. Behavior of REE and other trace and major elements during weathering of granite rocks, Evora, Portugal. Chemical Geology 107, 113–126.

Grousset, F.E., Biscaye, P.E., 2005. Tracing dust sources and transport patterns using Sr, Nd and Pb isotopes. Chemical Geology 222, 149–167.

Guo, L., Santschi, P.H., Baskaran, M., 1997. Interaction of thorium isotopes with colloidal organic matter in oceanic environments. Colloids and Surfaces, A 120, 255–271.

Halamic, J., Galovic, L., Sparica, M., 2003. Heavy metal (As, Cd, Cu, Hg, Pb and Zn) distribution in topsoil developed on alluvial sediments of the Drava and Sava Rivers in NW Croatia. Geologia Croatica 56 (2), 215–232.

Hamelin, B., Grousset, F.E., Biscaye, B.E., Zindler, A., 1989. Pb isotopes in trade wind aerosols at Barbados: the influence of European Emissions over the North Atlantic. Journal of Geophysical Research 94, 16243–16250.

Han, F., Banin, A., 1997. Long-term transformation and redistribution of potentially toxic heavy metals in arid-zone soils incubated: I. under saturated conditions. Water, Air, and Soil Pollution 95, 399–423.

Hansmann, W., Koppel, V., 2000. Lead-isotopes as tracers of pollutants in soils. Chemical Geology 171, 123–144.

Johnson, D.M., Hooper, P.R., Conrey, R.M., 1999. XRF analysis of rocks and minerals for major and trace elements on a single low dilution Li-tetraborate fused bead. Advances in X-ray Analysis 41, 843–867.

Keller, C., Domergue, F.-L., 1996. Soluble and particulate transfers of Cu, Cd, Al, Fe and some other major elements in gravitational waters of a podzol. Geoderma 71, 263–274.

Kirkwood, D.E., Nesbitt, H.W., 1991. Formation and evolution of soils from an acidified watershed: Plastic Lake, Ontario, Canada. Geochimica et Cosmochimica Acta 55, 1295–1308.

Klemme, S., Prowatke, S., Hametner, K., Gunther, D., 2004. Partitioning of trace elements between rutile and silicate melts: implications for subduction zones. Geochimica et Cosmochimica Acta 69 (9), 2361–2371.

Kump, L.R., Brantley, S.L., Arthur, M.A., 2000. Chemical weathering, atmospheric CO_2, and climate. Annual Review of Earth and Planetary Sciences 28, 611–667.

Kurtz, A.C., Derry, L.A., Chadwick, O.A., Alfano, M.J., 2000. Refractory element mobility in volcanic soils. Gelogy 28 (8), 683–686.

Kurtz, A.C., Derry, L.A., Chadwick, O.A., 2001. Accretion of Asian dust to Hawaiin soils: isotopic, elemental, and mineral mass balances. Geochimica et Cosmochimica Acta 65 (12), 1971–1983.

Langmuir, D., 1997. Aqueous Environmental Geochemistry, vol. 1. Prentice Hall, Upper Saddle Rive, NJ. 589 pp.

Lee, S.-Z., Chang, L., Yang, H.-H., Chen, C.-M., Liu, M.-C., 1998. Adsorption characteristics of lead onto soils. Journal of Hazardous Materials 63, 37–49.

Manga, M., 1998. Advective heat transport by low-temperature discharge in the Oregon Cascades. Geology 26, 799–802.

Melfi, A.J., Subies, F., Nahon, D., Formoso, M.L.L., 1996. Zirconium mobility in bauxites of Southern Brazil. Journal of South American Earth Sciences 9 (3/4), 161–170.

Middelburg, J.J., Weijden, C.H.V.D., Woittiez, J.R.W., 1988. Chemical processes affecting the mobility of major, minor and trace elements during weathering of granitic rocks. Chemical Geology 68, 253–273.

Nesbitt, H.W., Young, G.M., 1984. Prediction of some weathering trends of plutonic and volcanic rocks based on thermodynamic and kinetic considerations. Geochimica et Cosmochimica Acta 48, 1523–1534.

Nesbitt, H.W., Markovics, G., Price, R.C., 1980. Chemical processes affecting alkalis and alkaline earths during continental weathering. Geochimica et Cosmochimica Acta 44, 1659–1666.

Olson, K.W., Skogerboe, R.K., 1975. Identification of soil lead compounds from automotive sources. Environmental Science & Technology 9 (3), 227–230.

Othman, I., Al-Oudat, M., Al-Masri, M.S., 1997. Lead levels in roadside soils and vegetation of Damascus City. The Science of the Total Environment 207, 43–48.

Riebe, C.S., Kirchner, J.W., Finkel, R.C., 2003. Long-term rates of chemical weathering and physical erosion from cosmogenic nuclides and geochemical mass balance. Geochimica et Cosmochimica Acta 67 (22), 4411–4427.

Rudnick, R.L., Fountain, D.M., 1995. Nature and composition of the continental crust: a lower crust perspective. Reviews of Geophysics 33 (3), 267–309.

Sak, P.B., Fisher, D.M., Gardner, T.W., Murphy, K., Brantley, S.L., 2003. Rates of weathering rind formation on Costa Rican basalt. Geochimica et Cosmochimica Acta 68 (7), 1453–1472.

Taylor, A., Blum, J.D., 1995. Relation between soil age and silicate weathering rates determined from the chemical evolution of a glacial chronosequence. Geology 23, 979–982.

Teutsch, N., Erel, Y., Halicz, L., Chadwick, O.A., 1999. The influence of rainfall on metal concentration and behavior in the soil. Geochimica et Cosmochimica Acta 63 (21), 3499–3511.

Teutsch, N., Erel, Y., Halicz, L., Banin, A., 2001. Distribution of natural and anthropogenic lead in Mediterranean soils. Geochimica et Cosmochimica Acta 65 (17), 2853–2864.

Vitousek, P.M., et al., 1997. Soil and ecosystem development across the Hawaiian Islands. GSA Today 7, 1–8.

Wilcke, W., Krauss, M., Kobza, J., Zech, W., 2001. Quantification of anthropogenic lead in Slovak forest and arable soils along a deposition gradient with stable isotope ratios. Journal of Plant Nutrition and Soil Science 164, 303–307.

Wilkens, B.J., Loch, J.P.G., 1998. Accumulation of cadmium and zinc from diffuse immission on acid sandy soils, as a function of soil composition. Water, Air, and Soil Pollution 96, 1–16.